Instrumented splashdown testing of a scale model Titan Mare Explorer (TiME) capsule

R. D. Lorenz
ralph.lorenz@jhuapl.edu
K. Hibbard
Applied Physics Laboratory
Johns Hopkins University
Laurel
Maryland
USA

M. V. Paul, J. Walsh, D. W. Olds and S. Willits
Applied Research Laboratory
Pennsylvania State University
Pennsylvania
USA

E. B. Bierhaus and W. E. Kretsch
Lockheed Martin Space Systems Company
Littleton
Colorado
USA

ABSTRACT

Water entry tests are conducted with a scale model capsule to explore the sensitivity of splashdown accelerations and motions to impact conditions, to support estimation of splashdown loads and behaviours of the proposed Titan Mare Explorer (TiME) mission. A 3D printed capsule with off-the-shelf USB accelerometer loggers enabled tests to be performed on a tight schedule. Contact impulse and peak loads are presented for a range of impact speeds and geometries, and predicted loads at full-scale on Titan are derived. The observed variation of peak load with impact speed is broadly consistent with the theoretically-expected square law but is surprisingly also consistent with a linear function (in common with some results from the literature). Test execution procedures and the performance of the data acquisition system are reviewed.

Paper No. 4170. Manuscript received 11 March 2014, revised version received 6 December 2014, accepted 9 January 2015.

https://doi.org/10.1017/S0001924000010551 Published online by Cambridge University Press

1.0 INTRODUCTION

Splashdown, decelerating a returning space vehicle with hydrodynamic forces in water, is a convenient means of ensuring modest landing loads without having to provide airbags or retrorockets to mitigate the hard decelerations that land surfaces would otherwise introduce[1,2]. Splashdown is also the obvious means of delivering a vehicle to explore seas on other worlds, specifically the hydrocarbon seas on Saturn's moon Titan.

During the early development of the Huygens probe in the early 1990s, a prevailing model of Titan's surface was a global hydrocarbon ocean and thus landing in liquid was considered a likely scenario. Instrumentation was carried on the probe to measure liquids should the probe survive landing (not actually a mission requirement), and some basic splashdown dynamics analysis[3] was performed using the Von Karman momentum approach (also used in evaluating Mercury and Apollo some decades before). One instrumentation proposer[4] performed some early scale model tests into water, and some additional small-scale model testing[5] was performed with drops into water and into kerosene (as a room-temperature Titan liquid analog). Ultimately, however, Titan proved to be geographically diverse, and the Huygens probe landed – safely – in what turned out to be a pebble-strewn dry riverbed in Titan's equatorial deserts[6].

Titan's north polar regions, in contrast, have since been found to have hundreds of lakes, and three large seas. As reservoirs of organic materials of astrobiological interest, and as sites of oceanographic processes (such as air:sea gas exchange, the generation of waves, etc.) these seas are priority targets for future exploration.

One concept for the exploration of these seas is the Titan Mare Explorer (TiME), a proposal[7] to land a capsule in Titan's second largest sea, Ligeia Mare. This proposal was selected for a ten-month $3m Phase A study by NASA in May 2011. In connection with this study, we undertook a series of scale model splashdown tests to assess the likely splashdown loads, and to understand the splashdown phenomenology of our intended vehicle shape. These tests had to be conducted on an aggressive schedule (a couple of months), a constraint that substantially shaped our approach.

A principal objective of the tests was to determine the peak loads likely to be encountered, since the power source intended for the vehicle, an Advanced Stirling Radioisotope Generator (ASRG) had a specified landing load limit of 30g. Two such units would be accommodated near the centre of the capsule. The splashdown loads for TiME were to be simulated (using Titan sea parameters such as liquid density, which for liquid ethane and methane at Titan conditions is about 2/3 that of water on Earth) with Computational Fluid Dynamics (CFD) simulations. It was desired, however, to obtain data with which to validate such simulations, and to gain some visceral familiarity with the behaviour of the capsule at splashdown to facilitate interpretation of dynamics measurements made at Titan.

Physical testing complements CFD not only in capturing effects that occur at scales smaller than the numerical model resolution, but also in parametric sweeps. While a typical dedicated workstation can perform a splashdown contact simulation in about a day of computing time, the full resurge dynamics takes much longer execution time. In contrast, a physical scale model test – as we show here – can be executed in ten minutes or so. Because the likely range of impact speeds and angles was not well-constrained at the beginning of the Phase A study, it was considered useful to evaluate a rather wide range of parameters which was efficiently done with scale model tests.

https://doi.org/10.1017/S0001924000010551 Published online by Cambridge University Press

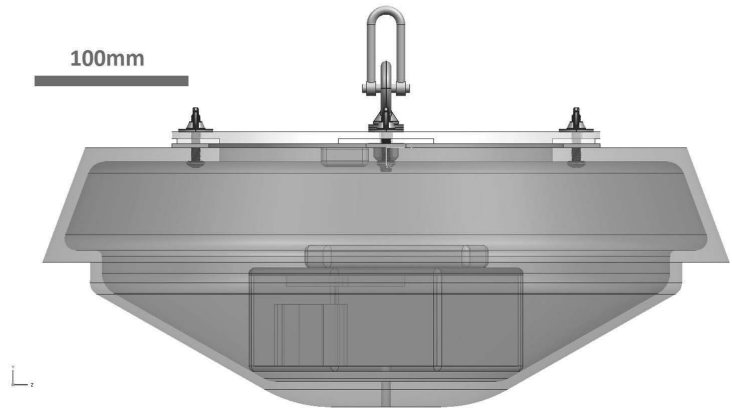


Figure 1. Semitransparent cross-section view of the test article.

2.0 TEST ARTICLE AND FACILITY

The TiME capsule, which had to accommodate a radioisotope power source, had a planned diameter D of ~3m, and would be expected to have an impact velocity $V = V_{imp}$ comparable with that of the 1·3m Huygens probe (~5ms^{-1}). Full-scale testing would be impractical. The capsule shape (Fig. 1) is similar to that of the Genesis and Stardust Earth-return capsules, being principally two back-to-back frustums with a small cylindrical section in between. The shape, and in particular a shelf just above the nominal waterline, is determined largely by the geometry of the jettisoned heat shield required for hypersonic entry.

Titan surface gravity g is 1·35ms^{-2}, or about 1/7th of Earth. Since dynamical similarity for liquid surface dynamics is achieved by matching the Froude number, i.e. $V/(gD)^{0.5}$, the behaviours for a given impact speed V would be matched on Earth and Titan with an Earth scale model test vehicle that is 1/7 the size of the full-scale Titan article (~3m). This was the guiding principle for the test model.

A logistical complication emerged on encountering this initial specification, in that the schedule limitations on the study favoured rapid manufacture via a 3D printing process. The fabrication facility (a fused deposition modelling (FDM) rapid prototype machine using an ABS plastic blend) had a maximum piece size which meant only a 1/8 scale model could be made as a single part – a 1/7 scale article (~35cm in diameter) would need to be made in two parts and joined. It was decided to proceed with a 1/8 scale model and adjust the impact speed slightly to match Froude number conditions.

The capsule model had a large circular hole in the aft surface in order to allow installation of instrumentation (see next section). A clear acrylic cover was attached across this hole using wing nuts for rapid access. The cover pressed against a rubber sheet gasket in order to achieve a waterproof seal. It was found that the 3D printed ABS model hull was not, in fact, watertight – the filament deposition 3D printing process allowed some considerable porosity, even with a hull thickness of ~0·5-1cm. Several layers of urethane lacquer were therefore applied to make the model hull watertight.

The tests were performed in the 25ft × 25ft water tank at the Applied Research Laboratory at The Pennsylvania State University. A custom drop rig was developed to deliver the capsule to the

https://doi.org/10.1017/S0001924000010551 Published online by Cambridge University Press

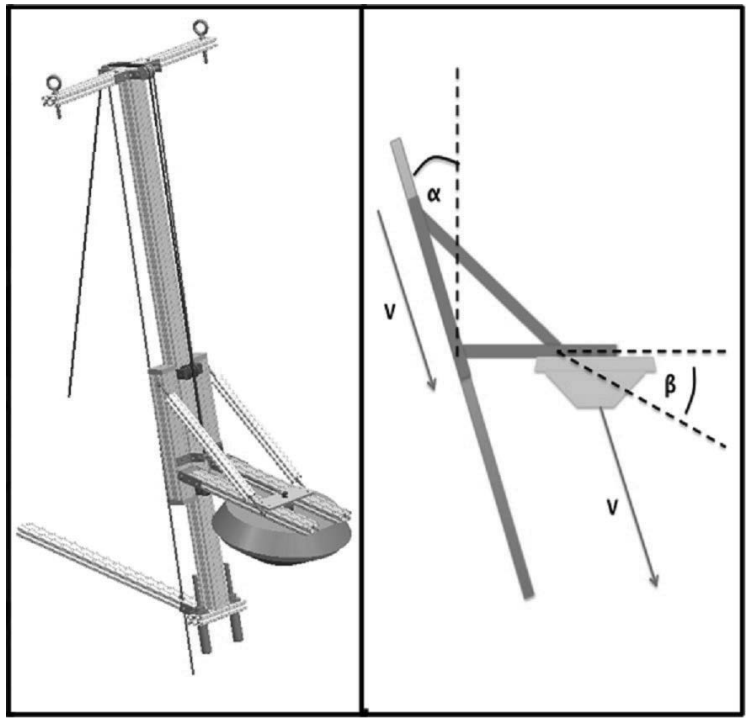


Figure 2. Sketch of the drop rig and impact geometry. The capsule is rigidly held on a carriage that slides down a rail. The drop height controls the release speed *V*, with the rail attachment controlling the flight path angle alpha, and the carriage geometry determining the angle of attack beta. Positive beta corresponds to leading-edge-down.

water surface at a known and reproducible vertical and horizontal velocity and attitude (Fig. 2). The drop rig consists of a rail, carriage, release mechanism, and velocity transducer. First, the model is pulled flush with the bottom of the carriage by the release mechanism. The carriage is then raised to the desired drop height using a rope, which is fastened to a quick-release shackle. A signal line to the shackle is pulled to initiate the drop, causing the carriage to slide down the rail. As the carriage falls it pulls the velocity transducer wire, the signal from which is recorded by the data acquisition system. Shortly before the carriage reaches the end of its travel, a mechanical stop triggers the release mechanism. The release mechanism consists of a lever that pulls a pin securing the model, allowing the model to free-fall as the carriage is arrested by a spring and damper system. Resetting the rig for a repeat drop requires only a few minutes. The probe, installed on the drop rig, can be seen in Fig. 3. The facility was equipped with two conventional video cameras to provide overall test documentation, as well as two high-speed cameras focused on the splashdown point to observe the capsule dynamics and fluid interaction (Fig. 4).

The carriage platform is mounted on hinges and positioned by tie rods. Varying the vehicle pitch attitude, β, ± 30 degrees entails changing the length of the tie rods and can be accomplished in as little as five minutes. Modifying the flight path angle, α, requires the gantry crane to translate the

https://doi.org/10.1017/S0001924000010551 Published online by Cambridge University Press



Figure 3. First author attaching the model to the release fixture on the launch rail.

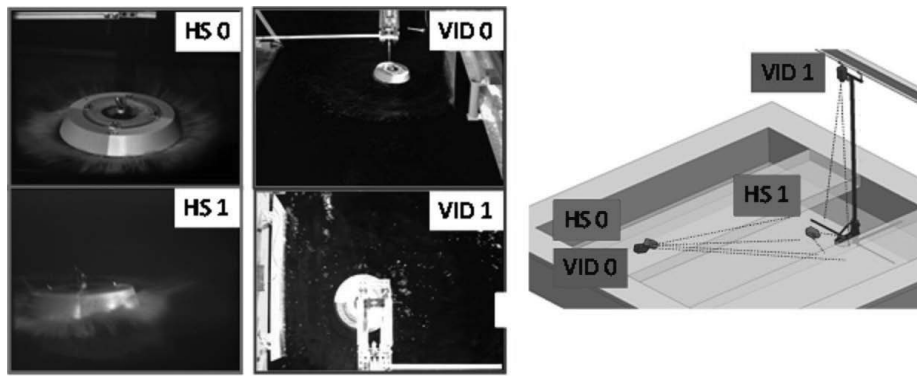


Figure 4. Video camera arrangement.

top of the drop rig while the bottom pivots on the lower braces. Extreme flight path angles, such as 30°, require a rail extension be bolted in place to keep the release point near the surface of the pool. Since the impact point changes with flight path angle, the various video cameras recording each event also required adjustment. This added complexity can cause a flight path angle change to take as long as 30 minutes. Mounting angles were verified with a digital protractor to within 2°, and while some slight distortion of the rail structure admitted a few degrees of roll, this was always less than 4°.

https://doi.org/10.1017/S0001924000010551 Published online by Cambridge University Press



Figure 5. The data acquisition hardware. At left is the X250 accelerometer logger with its cover removed (the X6, not shown, is similar) – its USB connector is visible. At right is the diecast box with the logger unit and ribbon cables to the rate gyros. The squares on the paper beneath are 5·2mm wide.

3.0 INSTRUMENTATION

The overriding objective in specifying the instrumentation was to execute the tests in the short timeframe available, and to capture the peak decelerations (expected to be some tens of g, with the impact event lasting ~D/V, a few tens of milliseconds). Secondary objectives were to characterise the resurge and bobbing motions. While high-speed video could be used to measure the impact conditions and resurge, measuring the peak loads required on-board acceleration measurements. To avoid applying cable loads and the risk of snagging, data acquisition and storage was to be performed onboard (Apollo work, and Huygens tests[4,5] used cabled data acquisition).

The solution selected, in part due to operator familiarity with the system, was a Gulf Coast Data Concepts (GCDC) X250 accelerometer logger. This unit is a microcontroller interfaced to an accelerometer and flash memory card, packaged in a small unit (about 1·5cm x 12cm – see Fig. 6) that functions as a USB memory stick. Data (three-axis accelerations up to 250g measured at 12 bits resolution at up to 512 samples per second) are stored as simple comma-separated-value (CSV) ASCII files that can be transferred by plugging the device into a PC, making the transfer of data fairly rapid. The unit is powered by a small lithium polymer (LiPo) battery that is recharged via the USB port. The pace of the test program did not admit any separate calibration effort, but the device specification (accelerometer linearity <2%, resonant frequency 10kHz) should have captured the event adequately.

Additionally a GCDC X6 accelerometer logger (with similar functionality, but a lower range and higher sensitivity) was installed to record bobbing and resurge (it was expected to be overranged by the splashdown contact itself). Finally, a Logomatic Data logger, was wired to two solid-state two-axis LP530AY angular rate sensors (and a third accelerometer, to facilitate synchronisation with the two other units). This unit records up to eight analog voltages (only five were used here,

https://doi.org/10.1017/S0001924000010551 Published online by Cambridge University Press

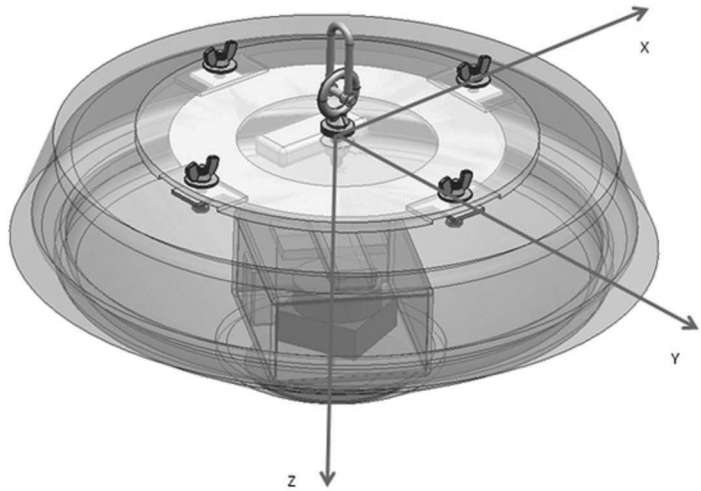


Figure 6. Semitransparent view of the capsule model. The diecast box is at lower centre, and the X6 logger just visible beneath the suspension lug on the acrylic lid. The X250 logger is mounted at the top of the diecast box, close to the centre of gravity of the capsule.

one for each gyro axis plus one accelerometer) as ASCII files that could be transferred by USB cable. This unit was also powered by a LiPo battery.

For rigid mounting in orthogonal axes and protection from damage and splash, the high-g logger and the gyro system were mounted with epoxy and screws respectively on a $12 \times 9 \times 6$cm die-cast aluminum box. The X6 logger was mounted on the underside of the acrylic lid (see Fig. 6). With the instrumentation, the capsule model had a mass of 2·7kg.

4.0 RESULTS

Around 80 tests were performed in the series described in this paper. Initially 3-4 personnel performed testing, although once procedures (such as data transfer, archiving of high-speed camera footage, as well as the mechanical execution of the test and the recovery of the capsule with a hook on the end of a broom handle) were refined, two persons could perform the tests efficiently. The test series was performed over about seven days in total, and over 90% of test drops yielded full datasets. Tests were conducted with impact speeds ranging from ~3·5 to ~9·5ms^{-1}, and at a range of impact angles.

4.1 Data characteristics and impact phenomenology

The high-speed video allowed close observation of the phenomenology of the splashdown (e.g. Fig. 7). Although in principle attitudes and positions could be measured (somewhat laboriously) from the video, this did not prove to be necessary as the speed measured by the pull-string was found to be very reproducible (such that a given drop height gave consistent release speeds) and the attitude did not change during free-flight (i.e. the tip-off angular impulse from the launch carriage was small enough not to be a concern).

https://doi.org/10.1017/S0001924000010551 Published online by Cambridge University Press

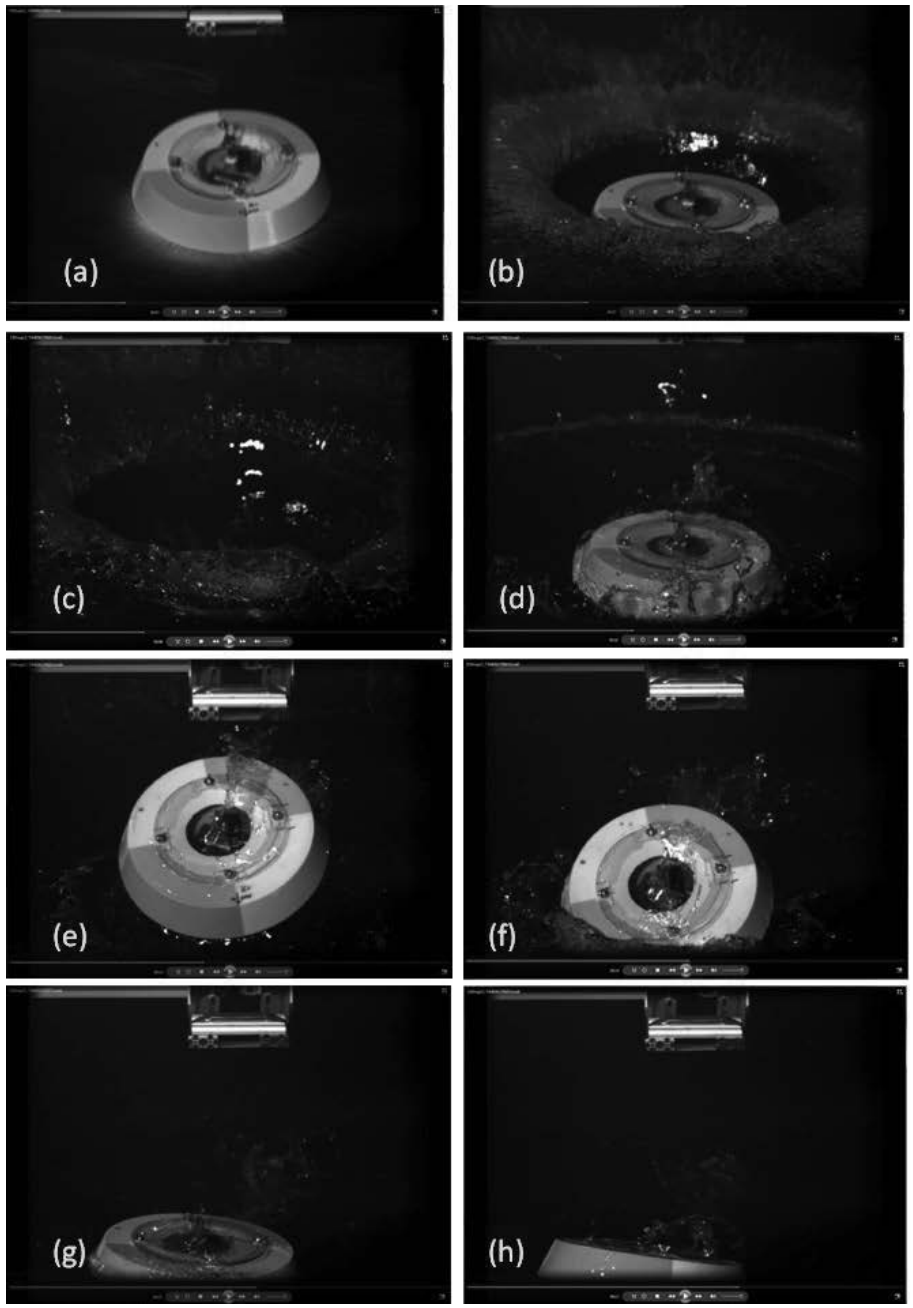


Figure 7. View from the downrange high-speed camera (HS 0), with frames about 100ms apart. The fact that the transient cavity is larger than the capsule is especially evident in frame (b). The fingering of liquid around the vehicle in frame (d) highlights the complex interaction of the fluid with the rim of the capsule. It is seen when comparing frames (c), which is approximately the deepest penetration of the capsule, and frame (f), a point during the resurge, that the upper surface of the capsule can become immersed not at deepest penetration, but during the fallback from the resurge bounce.

https://doi.org/10.1017/S0001924000010551 Published online by Cambridge University Press

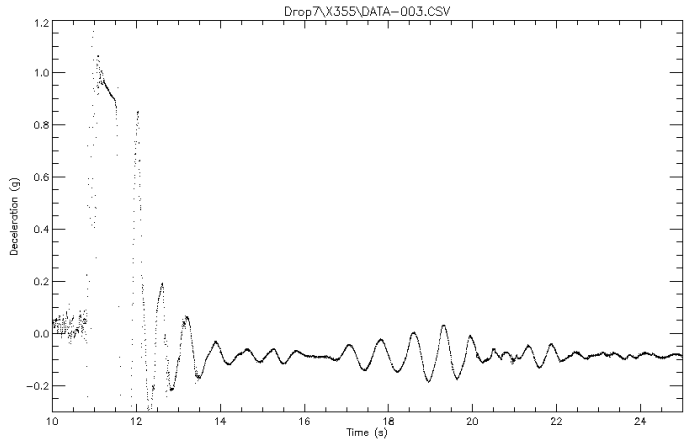


Figure 8. 15 seconds of X6 *Z*-axis data. Release at 11s, with the free-fall acceleration declining due to drag and friction. The contact event (negative tens of *g* at 11·7s) is off-scale. The resurge acceleration at 12s peaks at ~0·85g, and bobbing damps away over the next 3s. At 17s, 4s after contact, new motions are excited by the impact waves reflecting from the walls of the pool.

Of particular interest was the interaction with the liquid during first penetration, and the complex and energetic resurge behaviour. During impacts at normal incidence, after reaching the point of deepest penetration, the resurgence of the transient cavity would lift the vehicle almost back to the plane of the original surface, a behaviour nicknamed 'bounce'. For non-zero values of α or β, other dynamics occurred. The video allowed observation of the fluid interaction (e.g. whether liquid made contact with the upper surface of the vehicle – see Fig.7 panel (c)).

The accelerometer records were obtained generally as planned. The loggers record to one of two buffers which are alternately written to the nonvolatile flash memory. Recording is interrupted briefly when one buffer fills and the device switches to the other. On one or two occasions this happened during drop event itself (some ten or more minutes could elapse between when recording was started and the drop occurred) and so the event was not captured. Although data were acquired in three axes, only the axial (*Z*-axis, or axis of symmetry) loads were of particular interest.

The X-6 data (e.g. Fig. 8) show very clearly the acceleration phase on the launch rail, the release, free-flight and contact, and the subsequent dynamics, although (as expected) the contact phase has decelerations that saturated the instrument. It was observed (see also Fig. 9) that the acceleration phase was rather noisy (with variations of about 0·1-0·2g), due presumably to vibration on the launch rail due to imperfections in the rail and/or from the velocity transducer cable. It can be seen also that the acceleration declines by 0·1-0·2g during the descent, due to friction in the velocity transducer, air drag, and rail friction.

Features visible include the release of the carriage on the rail, sliding down the rail, release from the carriage and brief free-flight, structural ringing excited by the contact impulses, the resurge and subsequent bobbing (with slight discontinuities (Fig. 10) where the shelf hits or peels away from the water surface), and re-excitation of bobbing by waves reflected from the pool edge. The fact that these are readily distinguishable shows that the pool was large enough to avoid any edge effects on the dynamics of splashdown.

Large angular rates were recorded by the gyros (Fig. 11) and correspond to the pitch-up generally seen at contact, and the subsequent pitch-down during the resurge. These high rates, and the corresponding excursions in attitude were observed in scale model tests of Apollo capsules[8], and indeed of the actual flight Apollo capsules[9]. The rates, reaching ~300°/s or 5 radians/s cause

https://doi.org/10.1017/S0001924000010551 Published online by Cambridge University Press

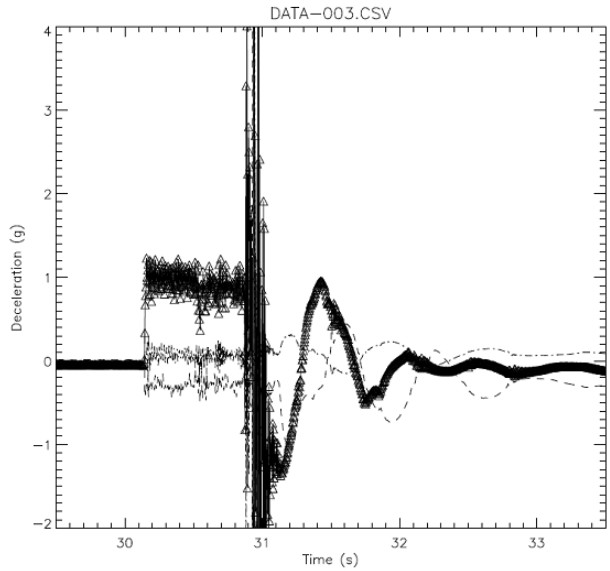


Figure 9. Closer view data from the X6 accelerometer logger. Triangles denote the *Z*-axis. These data have the initial bias values subtracted, and thus the initial reading is zero while the vehicle is at rest. Upon release at 30·15s, the vehicle begins free fall at 1g, declining slightly due to aerodynamic drag. The signal is very noisy during this phase as imperfections in the rail cause vibration. At 30·88 the vehicle is released (the transients from the pin retraction cause a brief large-amplitude reading) and undergoes a brief free flight. At 30·94s the vehicle hits the water and the readings are saturated. The data are again interpretable after about 31·1s, and show a damped bobbing, complicated by some discontinuities where the shelf hits the water surface (Fig. 10).

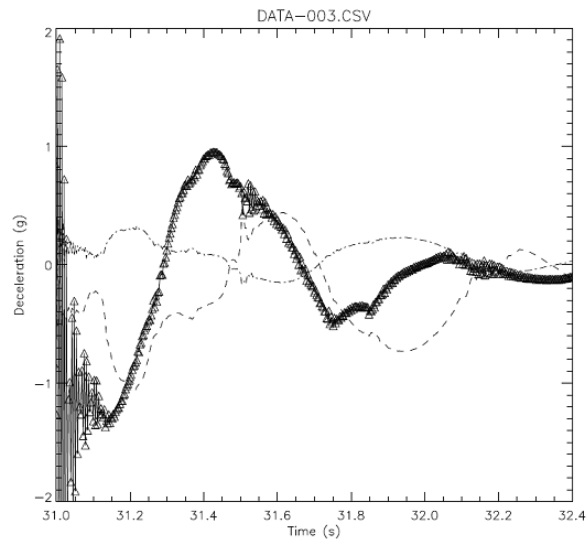


Figure 10. A zoom of Fig. 9. The decaying structural ringing is evident in the first ~0·2s of the record. Some additional high-frequency oscillations are excited at 31·5 and 32·1s, presumably when the shelf of the hull meets the surface, and at 31·8s where the shelf clears the water.

https://doi.org/10.1017/S0001924000010551 Published online by Cambridge University Press

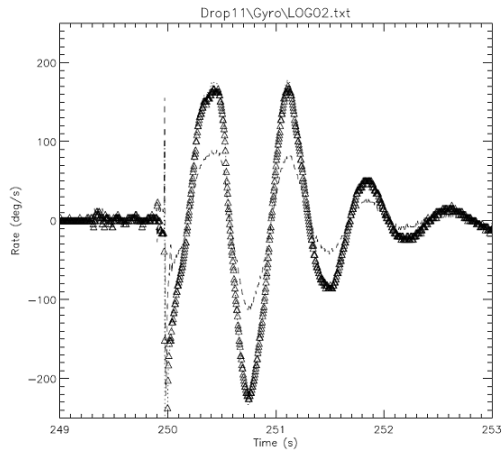


Figure 11. Gyro data. The vehicle experiences an instantaneous pitch-up (i.e. negative) moment at impact, jumping from zero to –200deg/s. As the vehicle resurges, however, it is smoothly accelerated in a pitch-down direction with a similar maximum rate. Successive pitch motions are progressively lower in amplitude.

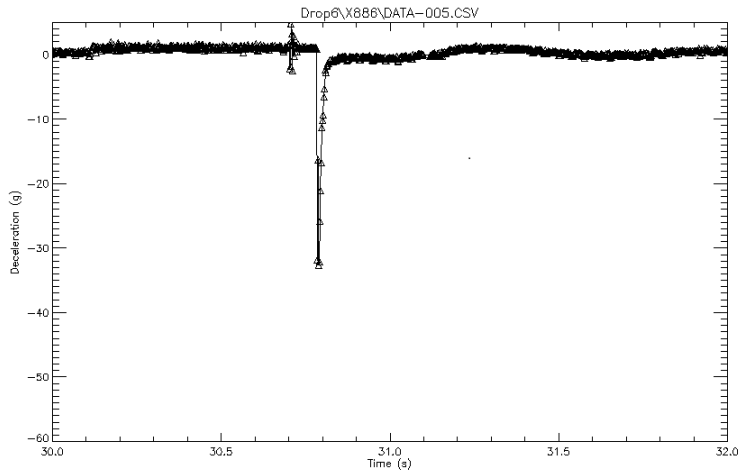


Figure 12. Overview of the X250 data showing the drop event (same drop and interval shown in Fig. 9). At 30·1s into the record the free fall begins and is just detectable as a step change. Note that the noise level recorded by this device is large (comparable with the ~1g difference between before and after release) due to the higher range of the accelerometer. At 30·6s a transient occurs at release and at 30·68s contact occurs. Two adjacent points show the peak deceleration during the contact pulse is reasonably well described. The contact transient is over by about 30·72s although the vehicle is still being accelerated upwards by drag and buoyancy until about 31·2s. Recall that the peak value seen here is for the scale model in 1g conditions; scaling for the Titan environment is discussed in Section 5.2.

a centripetal acceleration at the capsule lid (~0·1m above the centre of mass) of ~2·5g, a minor contribution to the sensed value.

Figure 12 shows the principal result sought in the tests, the peak loads experienced during the contact phase. Enlargement (Figs 13,14) show that the contact pulse is about 30ms long, and removes about 71% (see Fig.15) of the impact velocity, i.e. ~86% of the impact energy. The rest of the impact speed is arrested over about 300ms by near-constant buoyancy and drag.

https://doi.org/10.1017/S0001924000010551 Published online by Cambridge University Press

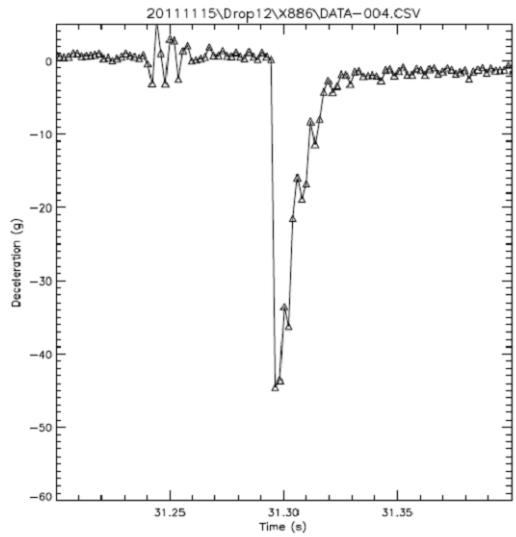


Figure 13. Close view of the X-250 *Z*-axis data at the instant of splashdown. Two samples with nearby values suggest the peak deceleration has been reasonably well captured, although some structural ringing is evident in the subsequent record. The transient at 31·25s is the release from the carriage. Here a peak deceleration of ~45g is indicated, with an initial ringing amplitude of 2-3g. The ringing at release from the carriage has a similar amplitude.

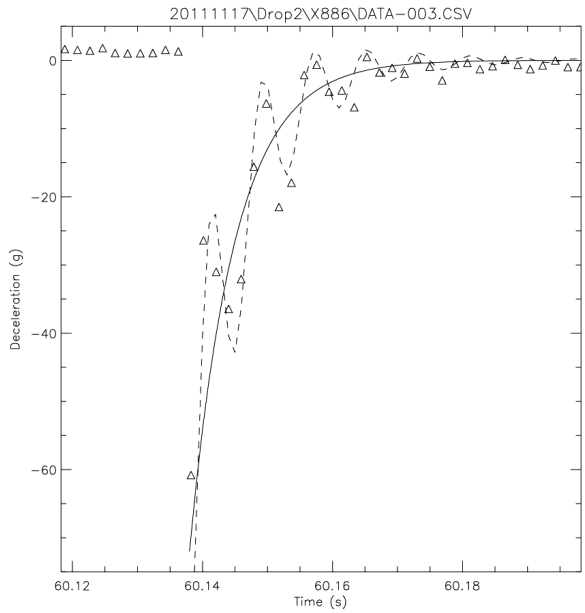


Figure.14. An extreme zoom of the data points recorded at the contact event in Fig. 13. An exponential curve is shown as representative of the evolution of the rigid-body deceleration during the contact event (~20ms long), whereas a dashed curve has a decaying sinusoid superposed on the exponential, describing a structural oscillation with a period of ~5ms.

https://doi.org/10.1017/S0001924000010551 Published online by Cambridge University Press

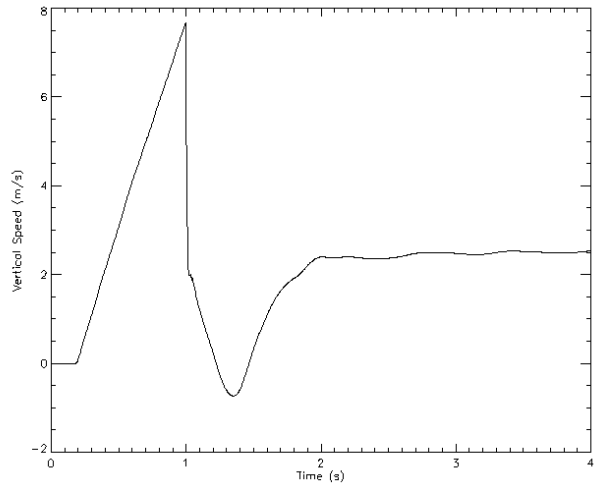


Figure 15. Integrated record from the X250 accelerometer showing the velocity history. The near-linear acceleration down the rail (0·2-1s) is evident, as is the sharp near-vertical drop in speed at contact (1s), and the subsequent smooth variation during resurge. Because the measurement is in the body-fixed frame uncorrected for rotation, the final integral speed is not zero. It is clear that about 6ms^{-1} of velocity (i.e. ~75%) is near-instantaneously removed by the impulse at contact.

4.2 Results – peak deceleration

A principal result is the 'raw peak' deceleration recorded in each test, which is readily extracted from the record by looking for the maximum value in the *Z*-axis deceleration history. However, as noted in prior investigations of scale model splashdown tests (e.g. Ref. 8), this may under- or over-predict the characteristic deceleration of the vehicle due to the superposition of structural oscillations. Thus a general approach is to derive a 'faired' acceleration, historically a smooth curve drawn by hand using engineering judgment. Such an approach would be subjective, and given our large dataset, laborious.

The sampling rate of 512Hz is just enough to resolve ringing (typically at ~200Hz, Fig. 13), and a model described by six parameters (a peak deceleration, a decay time, a ringing magnitude, frequency, decay time and phase relative to the deceleration peak) is seen to describe the record well. However, there are only about 15 data points before the record decays into noise, and so this six-term model is not robustly constrained in all parameters, not all of which are of interest anyway. Thus to avoid over fitting, and to permit an analysis robust enough to be performed automatically, we adopt the following procedure.

We integrate the acceleration signal from the jump at contact to the point where the deceleration decays to 5g or less: this defines the duration of the contact phase. The integral over this period represents the velocity lost during the contact impulse ('ΔV') and corresponds to the sharing of impact momentum with an added mass of liquid before drag and buoyancy have had time to act appreciably. Dividing the velocity loss by half the contact pulse duration defines a faired deceleration, essentially describing the record as a triangular pulse. Low-pass filtering of the data was attempted, but did not yield obviously more reproducible results, and may in any case underestimate the peak loads.

https://doi.org/10.1017/S0001924000010551 Published online by Cambridge University Press

Table 1
Reduced test results

Impact Speed (ms^{-1})	Alpha (°)	Beta (°)	Peak Deceleration (g)	Impulse Duration (s)	Delta-V (ms^{-1})	Faired Deceleration (g)
3·6	0	0	24·08	0·0234	2·94	25·61
3·64	0	0	37·53	0·0215	2·64	25·07
4·23	0	0	42·29	0·0254	3·71	29·82
4·77	0	0	54·6	0·0234	3·77	32·77
5·33	0	0	44·96	0·0254	4·52	36·27
5·4	0	0	50·67	0·0273	4·27	31·87
5·85	0	0	32·65	0·0215	4·19	39·8
5·93	0	0	70·07	0·0215	4·2	39·86
6·18	0	0	74·87	0·0234	4·8	41·71
6·52	0	0	51·02	0·0215	4·92	46·66
7	0	0	47·24	0·0215	5·41	51·3
7·2	0	0	46·98	0·0215	5·18	49·17
7·23	0	0	50·1	0·0215	4·79	45·47
7·95	0	0	51·24	0·0234	5·53	48·14
5·96	0	–10	42·86	0·0215	4·16	39·5
7·09	0	–10	45·95	0·0234	5·2	45·21
7·15	10	0	60·81	0·0234	4·98	43·34
3·6	0	–15	20·35	0·0215	2·33	22·07
5·4	0	–15	48·92	0·0234	3·84	33·43
7·13	0	–15	44·08	0·0234	4·97	43·26
5·75	0	–20	47·66	0·0234	3·8	33·03
7·33	0	–20	57·76	0·0254	5·25	42·17
3·5	10	–10	23·32	0·0234	2·61	22·74
5.13	10	–10	38·75	0·0234	3·61	31·37
6·8	10	–10	52·77	0·0234	4·91	42·69
7·04	20	0	78·75	0·0234	5·33	46·36
7·41	20	0	55·82	0·0215	5·31	50·35
7·48	20	0	52·04	0·0234	5·26	45·73
3·56	10	10	20·92	0·0215	2·68	25·44
5·26	10	10	31·7	0·0234	4·1	35·64
6·9	10	10	44·12	0·0215	5·01	47·56
5·83	0	–30	48·73	0·0293	3·94	27·39
6·72	0	–30	62·37	0·0293	4·41	30·67
6·82	0	–30	111·9	0·0293	4·81	33·49
7·87	0	–30	68·96	0·0313	5·17	33·74
3·57	10	–20	20·19	0·0215	2·22	21·07
5·36	10	–20	35·74	0·0254	3·57	28·67
7·11	10	–20	59·44	0·0254	4·74	38·04
7·99	10	–20	57·23	0·0313	5·87	38·27
8	10	–20	67·28	0·0254	5·07	40·73
8·03	20	10	56·54	0·0215	5·15	48·87

https://doi.org/10.1017/S0001924000010551 Published online by Cambridge University Press

Impact Speed (ms^{-1})	Alpha (°)	Beta (°)	Peak Deceleration (g)	Impulse Duration (s)	Delta-V (ms^{-1})	Faired Deceleration (g)
3·6	0	30	41·15	0·0293	2·65	18·44
5·7	0	30	48·35	0·0273	4·51	33·64
5·75	0	30	54·83	0·0313	4·7	30·66
5·79	0	30	86·53	0·0254	4·32	34·69
7·33	0	30	60·46	0·0313	5·86	38·25
5·46	20	–20	47·23	0·0215	4·24	40·27
5·48	20	–20	40·23	0·0273	4·22	31·44
5·53	20	–20	45·76	0·0293	4·2	29·2
7·7	20	–20	41·49	0·0273	4·41	32·91
7·7	20	–20	51·97	0·0273	4·64	34·58
7·49	30	–10	28·42	0·0273	4·31	32·16
5·29	10	30	56·27	0·0234	3·76	32·75
7	10	30	106·57	0·0273	5·21	38·83
7·95	10	30	108·97	0·0254	5·25	42·16
3·22	30	30	33·72	0·0215	2·23	21·12
4·67	30	30	40·65	0·0254	3·41	27·41

We plot these derived parameters, listed in Table 1, against impact speed in Figs 16-18. Unsurprisingly, the peak deceleration increases with impact speed (Fig. 16), although the scatter in the data is rather high, with variation over a factor of about 4 (presumably in part because structural ringing is more strongly excited at higher impact speeds). A straight line describes the data reasonably well, $a_{max} \sim 6 V_{imp}$, although on theoretical grounds one would expect the peak to be proportional to the square of velocity, and thus a relationship $a_{max} \sim 0{\cdot}75 V_{imp}^{\ 2}$ might be preferred. The scatter in the data, however, make it difficult to discriminate between these functions. The envelope that is never exceeded by the points (arguably a parameter of particular interest, with the caveat that structural oscillations may not straightforwardly scale up to the actual vehicle) is quite clearly concave upwards, and is described well by $a_{max} \sim 2{\cdot}5 V_{imp}^{\ 2}$.

We now examine the 'faired' deceleration value (Fig. 17). As intended, the scatter in this quantity is less (~20%) than for the raw peak values (~100%). The functional form appears, surprisingly, quite linear, with a value of $\sim 5{\cdot}86 V_{imp}$. It seems that this proportionality results from the impulse removing a more or less constant fraction of the impact velocity – as shown in Fig. 18, $\Delta V = 0{\cdot}71 V_{imp}$. We discuss the velocity dependence of peak deceleration in a later section.

Figures 19 and 20 shows the dependencies of the raw peak and faired peak decelerations on the flight path angle alpha and the angle of attack beta. The faired deceleration is insensitive to alpha : this is consistent with the ¼-scale Apollo tests of Stubbs[8] who found data for different horizontal velocities (i.e. alpha) collapsed onto the same curve. Interestingly, we find the highest raw peak values for high alpha. One possibility is that the structural oscillations that affect the raw peak are highest for off-normal impacts (which explains the increase in scatter as well as the increase in maximum value.)

https://doi.org/10.1017/S0001924000010551 Published online by Cambridge University Press

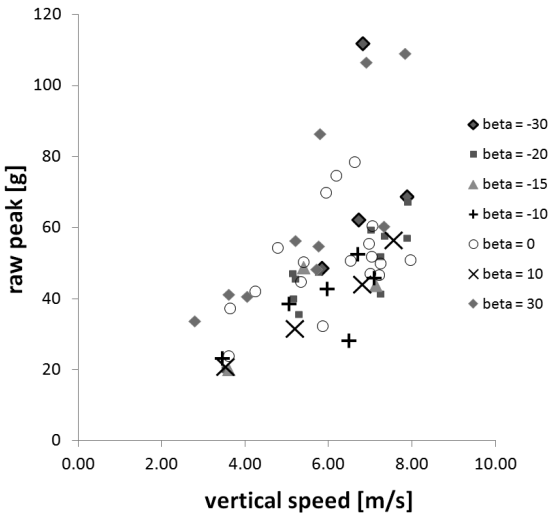


Figure 16. The raw peak deceleration has a scatter that is uncomfortably large. However, it is notable that the largest values (and the largest scatter) are for beta = 30 (i.e. 30 degrees nose-down), perhaps due to a 'slap' effect described in the text. An additional cluster of beta = 0 points (dashed oval) may have a similar cause. An acceleration of ~2·5V_{imp}^2 is not exceeded in any instance.

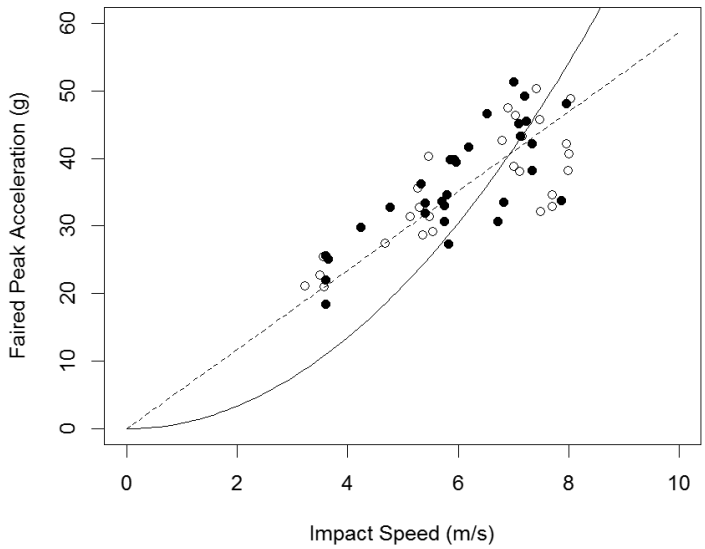


Figure 17. The faired deceleration (the peak of a triangular deceleration pulse with width and total area, i.e. ΔV, equal to that observed) has a rather reduced scatter, of about ±20%, and varies as $A_f = 5{\cdot}86V_{imp}$ (dashed line, $R^2 = 0{\cdot}979$). The correlation ($R^2 = 0{\cdot}93$) of the expected quadratic dependence (best fit is $A_f = 0{\cdot}846\ V_{imp}^2$, solid curve) is in fact rather poorer. None of the data (filled points correspond to Beta = 0) exceeds $A_f = 7{\cdot}5V_{imp}$.

https://doi.org/10.1017/S0001924000010551 Published online by Cambridge University Press

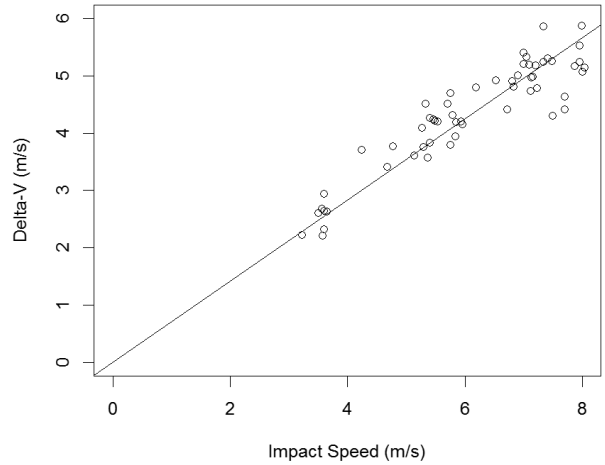


Figure 18. The impulsive velocity decrement ('*Delta-V*') at impact is rather linear and points to the origin with a relation of $\Delta V = 0{\cdot}707 V_{imp}$ ($R^2 = 0{\cdot}99$).

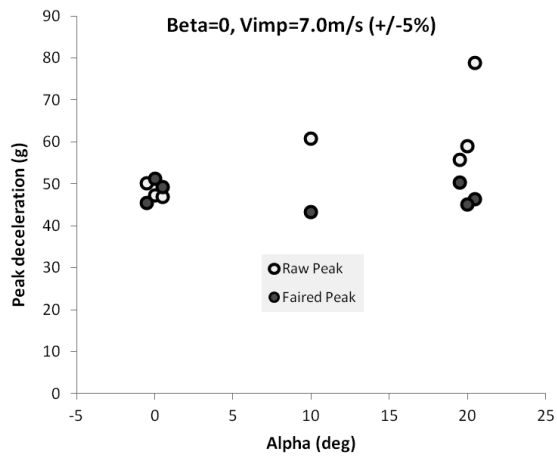


Figure 19. At zero angle of attack (beta = 0) and a constant impact speed, the faired peak deceleration is insensitive to flight path angle (alpha) but the raw peak value increases and increases in scatter. (Points are offset by 0·5 degrees in alpha for presentation purposes).

A similar effect is noted (Fig. 20) for the angle-of-attack dependence - the scatter and maximum value of the peak deceleration increases for higher angles. There does appear to be a consistent effect of angle-of-attack on the faired peak – it falls off as the square of the cosine of beta. One issue is that the accelerometer component is no longer in the velocity direction, accounting for one cosine factor. The other presumably arises because the flat front of the capsule no longer slaps onto the water, but the conical edge of the frustum knifes into the water, reducing the peak

https://doi.org/10.1017/S0001924000010551 Published online by Cambridge University Press

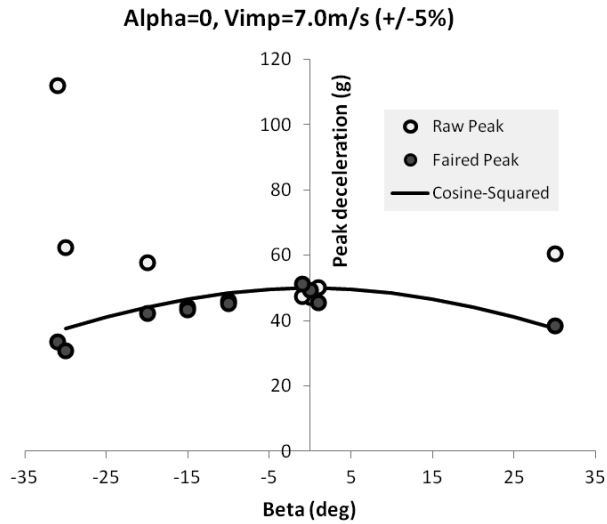


Figure 20. The dependence of faired peak on angle-of-attack is more systematic, varying roughly as the square of Cos(Beta).

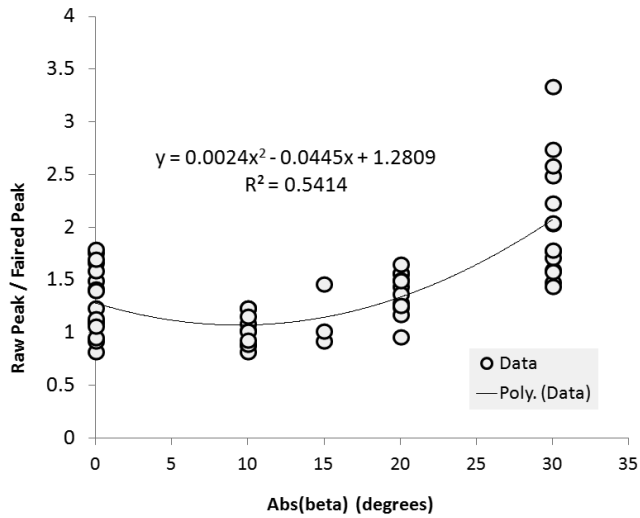


Figure 21. The ratio of raw peak to faired peak shows increased scatter towards beta = 0 (where the flat nose of the capsule impacts normally) and towards beta = 30 (where the conical surface of the capsule impacts). The scatter is a minimum around beta ~10 degrees, where the nose edge knifes into the water.

deceleration. (It was for this reason that the Apollo capsule was suspended so that the edge of the heat shield knifed into the water, and Stubbs' data shows a strong fall-off of peak deceleration for greater pitch attitudes). This effect is seen in Fig. 21, where the ratio of raw peak deceleration to faired peak is plotted against beta. This ratio shows considerable scatter (generally towards higher values) at beta~0 (nose slap) and towards beta~30 (slap of the conical surface), with a minimum around beta~10, where the capsule nose somewhat knifes into the water and is less sensitive to the presence or otherwise of ripples.

https://doi.org/10.1017/S0001924000010551 Published online by Cambridge University Press

5.0 DISCUSSION

5.1 Test procedure

The rig system worked well and reproducibly. Small changes in alpha were easy to implement by nudging the upper attachment points of the launch rail (via a remote-control gantry): the lower attachment point could be loosened to allow enough compliance for this adjustment.

Changes in angle of attack were accomplished by loosening several bolts and sliding the attach rail into a new position. This typically took 10 minutes or so.

The capsule release was effected by a cam which was rotated by impact with a protruding bolt head on the launch rail. The cam pulled a lanyard which retracted a bolt holding the capsule onto the attach rail. After some two hundred tests or so (in a separate uninstrumented test series to be reported elsewhere – a longer test series than was originally anticipated), some wear on the cam was noted, and the cam axle was observed to be bent and had to be replaced.

Some areas where attention might be devoted in future developments include

- Stiffer carriage platform to prevent inadvertent roll angle
- Vibration resistant fasteners
- Stronger tie rod brackets to prevent damage
- Redesign tie rods for faster pitch changes
- Redesign rail extension for faster flight path angle changes
- Experiment with dampers and springs for softer carriage landing
- Custom velocity transducer with longer wire, or other improved means of measuring carriage velocity.

The removal of the cover and download of data took several minutes. While it was useful to verify successful data acquisition after each test, in fact the data acquisition systems used would allow sampling for several hours before the batteries became depleted or memory filled. Thus in principle a series of dozens of tests could be conducted without the dismantling/download/reassembly step, and data related to test conditions via timestamps in one long record. Such an approach would increase the test execution rate by a factor of several, albeit with a greater risk of losing data due to undetected malfunction and with slightly larger effort in locating events in the data sequence.

5.2 Accelerations – predictions for Titan

The momentum theory of water impact was investigated (for seaplane floats) by Von Karman, and applied (via numerical calculation) to the Mercury and Apollo capsules (see e.g. reviews of water entry by Lorenz (1994)[3] and Seddon and Moatamedi (2006)[2]). For simple shapes penetrating a liquid, the equations can be solved analytically (e.g. the succinct solutions of Hirano and Miura, (1970)[11]) to derive the peak loads. For a spherical nose the peak deceleration A_{max} can be written

$$A_{max} = kF^2\mu^{-0{\cdot}667}g$$

The two dimensionless parameters here are a relative density $\mu = (3M_o/4\pi\rho R_N^3)$ and the Froude number $F = V_{imp}/(gR_N)0{\cdot}5$ with R_N the nose radius, ρ the density of the liquid, and M_o the mass of the vehicle. The prefactor $k = 0{\cdot}491$ (in their derivation, $(256/243)\pi^{-0{\cdot}667}$) has no fundamental

https://doi.org/10.1017/S0001924000010551 Published online by Cambridge University Press

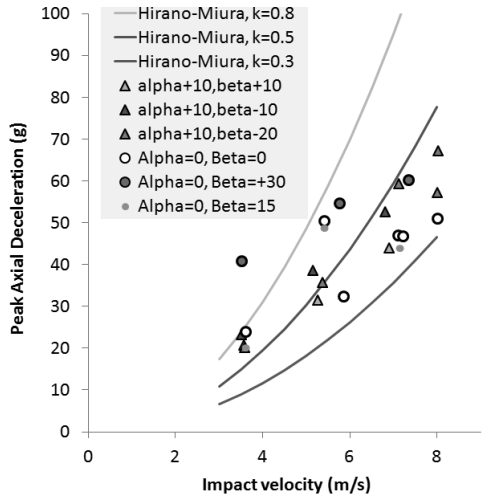


Figure 22. Hirano-Miura scaling shows that the raw peak values are bounded by the model predictions for k.

significance generally – Hirano and Miura obtain it on the assumption of the analytic added mass of a hemisphere. Seiff *et al* (2005) found that peak loads into water for a 1/9 scale Huygens probe model were described by $0{\cdot}49 < k < 0{\cdot}6$ but a 1/3 scale model showed more scatter and ranged $0{\cdot}49 < k < 0{\cdot}8$.

When we plot some example data (Fig. 22), we find that the scaling (using the model radius $R_N = 0{\cdot}18$m, representative of the overall capsule size) yields results that are reassuringly of the correct magnitude for $0{\cdot}3 < k < 0{\cdot}8$, with $0{\cdot}3 < k < 0{\cdot}5$ bounding the data at the relevant Froude number. In principle, the flat nose of the model is effectively an infinite nose radius, but in practice off-normal impact and the presence of ~cm amplitude ripples in the surface of the liquid suppress this singularity.

We can use the scaling, then, to predict the impact loads of the full-scale vehicle at Titan. There, the density of liquid ethane at 94K gives $r = 650\text{kg/m}^3$, $g = 1{\cdot}35\text{ms}^{-2}$. For the purpose of exposition and similarity with the scale model, we assume $R_N = 1{\cdot}5$m and M_o~650kg. This then yields peak decelerations of 5·5g-9g for $k = 0{\cdot}3$-$0{\cdot}5$, which is comfortably lower than the 30g limit for the ASRG.

5.3 Accelerations – velocity dependence

The apparent deviation of the peak deceleration from the expected velocity-squared dependence in our tests is somewhat unsettling given the overall success, and obvious physical pedigree, of the momentum theory (e.g. Refs 2 and 3). However, we find the square law behaviour is in fact also not reliably demonstrated in other tests in the literature.

Hirano and Miura[11] only present three impact speeds, and while the data appear consistent with their theory, the upward-concavity of the data is not actually as strong as the model would require (the same pattern we observe). Somewhat linear behaviour is seen in small-scale Huygens model drops into kerosene and into water in tests by Lorenz[5]. Similarly, the data of Seiff *et al*[4] appear to be almost as well described by a straight line as a quadratic in impact speed (see Fig. 23). Wilkinson[12] presents some results from full-scale Apollo tests in 1967 (Fig. 24) that show some convexity, but again the data seem to be almost linear with impact speed. However, it is of note that both these datasets provide poorer fits to a linear model if the line is forced through the origin.

https://doi.org/10.1017/S0001924000010551 Published online by Cambridge University Press

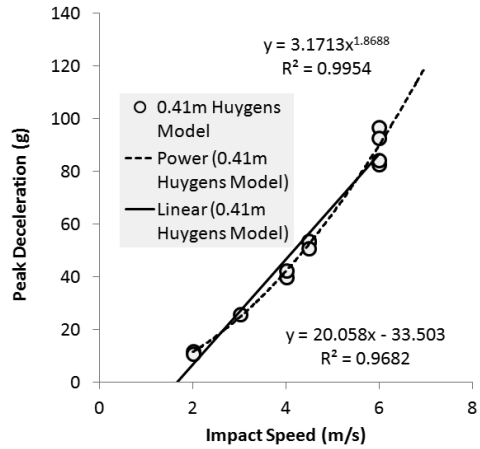


Figure 23. Peak decelerations on a scale model Huygens probe drop-tested into water in the late 1980s by the late Alvin Seiff at NASA Ames[4]. Although a power law fit of peak deceleration *vs* velocity yields an exponent close to 2·0 as expected from theory, in fact the convexity of the points is not large and a linear fit is nearly as good. However, forcing the linear fit to pass through the origin yields a much poorer fit (R^2 = 0·83).

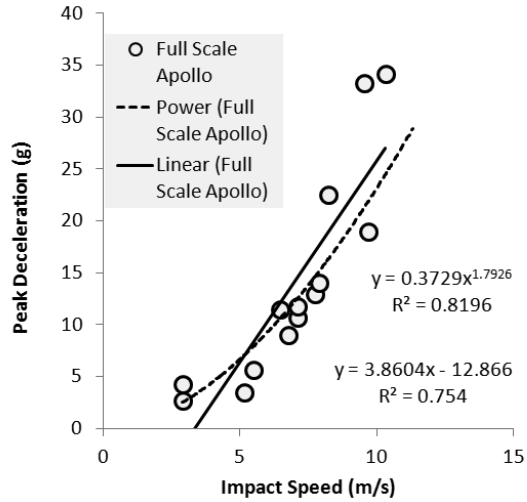


Figure 24. Peak decelerations measured on a full-size Apollo capsule during tests at North American Aviation[12]. Although these data alone are not much better fit by a quadratic or power law than by a linear function, again forcing the linear fit to pass through the origin leads to a much poorer correlation (R^2 = 0·59).

A full investigation of these possible deviations from theory is beyond the scope of the present paper. One possibility is that the timescale of the impulse (during which the capsule shares its momentum with the added mass of liquid) is assumed in theory to be inversely proportional to impact speed. Physically this requires an undisturbed liquid surface during the penetration, and the interaction time is simply some scaling dimension (typically nose radius) divided by impact

https://doi.org/10.1017/S0001924000010551 Published online by Cambridge University Press

speed. For a flat-bottomed vehicle, as here, the interaction time is zero and the growth rate of the added mass, and thus the impact force, is formally infinite for a perfectly normal impact onto a perfectly flat surface; in practice the force may be limited by speed of sound, or possibly by the presence of small waves in the liquid surface. (While gross waves – see Fig. 8 – died down between tests, some small capillary waves were always present as a result of ventilation airflow etc.) Inspection of table 1 shows the impulse duration is largely constant – the variation in faired peak deceleration is due principally to the proportional change in impulse with impact speed rather than a change in the duration).

6.0 CONCLUSIONS

We have deduced peak splashdown loads on Titan of 5·5-9g based on analytic Froude scaling of model test results, meeting the principal objective of our tests. The raw peak value, which appears to be contaminated by structural oscillations, shows a large variation with speed (bounded by the square of speed, and increasing with increasing flight path angle and angle of attack). A faired peak axial deceleration (believed representative of the rigid-body loads) showed less scatter, but a surprising proportionality to speed, and to the squared cosine of the angle-of-attack. The choice between linear and quadratic fits to our data (and some in the literature) is somewhat equivocal, although the expectation from momentum theory is that a quadratic dependence should be seen. It is possible the flat-bottomed shape of our vehicle, and the possible presence of capillary waves in the test tank, are factors in our measurements.

The availability of inexpensive off-the-shelf data loggers with built-in accelerometers and flash memory makes it easy to acquire high-fidelity data in scale model tests, although for the conditions in our test, the sample rate of 512Hz was only marginally able to resolve the impulsive peak of the flat-nosed capsule (a round-nosed capsule would have had impulses with a longer rise time). Additive manufacturing is a conveniently rapid means of constructing scale models, although additional waterproofing may be necessary. Construction and adjustment of a structure to control the impact conditions may be the rate-limiting step in initiating and conducting a series of tests. Some interesting non-monotonic behavior of peak loads (and peak/faired load ratio) has been noted: some independent documentation of the presence and/or amplitude of waves in the water surface might be useful in the interpretation of this effect.

The most time-consuming elements in each test run were the disassembly and reassembly of the model to access the interior to download data from each test, and the various start-stop and file-handling operations associated with several high-speed cameras. If on-board memory and camera disk space permit, and confidence in data acquisition and timetagging is sufficiently high, test series could be executed rather more quickly by taking data continuously and extracting individual records afterwards.

ACKNOWLEDGEMENTS

We are grateful for the comments of two referees: Referee 2 exposed some unpublished data to us which we found reassuring. The preparation of this paper was supported by a Janney Publication Fellowship to RL from the JHU Applied Physics Laboratory. Parts of this work were supported by NASA, and parts by internal support from the Applied Physics Laboratory, the Applied Research Laboratory, and Lockheed Martin. Dr Ellen Stofan was the Titan Mare Explorer Principal Investigator.

https://doi.org/10.1017/S0001924000010551 Published online by Cambridge University Press

REFERENCES

1. FASANELLA, E.L. Multiterrain earth landing systems applicable for manned space capsules, American Society of Civil Engineers, *J Aerospace Eng*, 2009, **22**, pp 201-213.
2. SEDDON, C.M. and MOATAMEDI, M. Review of water entry with application to aerospace structures, *Int J of Impact Engineering,* 2006, **32**, pp 1045-1067.
3. LORENZ, R.D. Huygens probe impact dynamics, *ESA J*, 1994, **18**, pp 93-117.
4. SEIFF, A., STOKER, C.B., YOUNG, R.E., MCKAY, C.P. and LORENZ, R.D. Determination of the physical properties of a planetary surface by acceleration measurements at impact, *Planetary and Space Science*, 2005, **53**, pp 594-600.
5. LORENZ, R.D. Splashdown and post-impact dynamics of the Huygens probe: Model studies, 2003, *Proc of Int Workshop on Planetary Entry and Descent Trajectory Reconstruction and Science*, pp 117-124 Lisbon, Portugal, October 2003, ESA SP-544, European Space Agency, Noordwijk, The Netherlands.
6. LORENZ, R.D. and MITTON, J. *Titan Unveiled*, Revised Paperback Edition, 2010, Princeton University Press.
7. STOFAN, E.R., LORENZ R.D., LUNINE J.I., BIERHAUS, E.B., CLARK, B., MAHAFFY, P. and RAVINE, M. TiME − The Titan Mare Explorer, March 2013, Paper 2434, IEEE Aerospace Conference, Big Sky, MT, USA, doi:10.1109/AERO.2013.6497165.
8. STUBBS, S.M. Dynamic model investigation of water pressures and accelerations encountered during landings of the Apollo spacecraft, September 1967, NASA Technical Memorandum, TN D-3980, NASA.
9. LORENZ, R.D. Apollo capsule capsize stability during splashdown: Application of a cavity collapse model. *J British Interplanetary Society*, 2011, **64**, pp 289-295.
10. WIERZBICKI, T. and YUE, D.K. Impact damage of the Challenger crew compartment, *J Spacecraft and Rockets*, 1986, **23**, pp 646-654.
11. HIRANO, Y. and MIURAK, K. Water impact accelerations of axially symmetric bodies, *J Spacecraft and Rockets*, 1970, **7**, pp 762-764.
12. WILKINSON, J. Study of Apollo water impact Final Report Volume 4 − Comparison with experiments, May 1967, North American Aviation, SID 67-498, Published as NASA CR-92022.

https://doi.org/10.1017/S0001924000010551 Published online by Cambridge University Press